JOURNAL OF MATERIALS SCIENCE **37** (2002) 1887– 1893

Thermal evolution of $Fe_{62.5}Co_6Ni_{7.5}Zr_6Nb_2Cu_1B_{15}$ metallic glass

F. BRANDA, G. LUCIANI, A. COSTANTINI
Dipartimento di Ingegneria dei Materiali e della Produzione, Università di Napoli "Federico II", Napoli, Italy

P. SCARDI
Dipartimento di Ingegneria dei Materiali, Università di Trento, Trento, Italy

L. LANOTTE, A. D'AGOSTINO
Istituto Nazionale per la Fisica della Materia (INFM), Dipartimento di Scienze Fisiche, Università di Napoli "Federico II", Napoli, Italy

Thermal evolution of $Fe_{62.5}Co_6Ni_{7.5}Zr_6Nb_2Cu_1B_{15}$ amorphous alloy prepared by one-roll melt-spinning technique was studied by XRD and DTA. The crystallisation process, occurring in several steps, can be summarised as follows: $a \rightarrow a' + \alpha$-Fe $\rightarrow a'' + \alpha$-Fe $+ \gamma$-Fe $\rightarrow \alpha$-Fe $+ \gamma$-Fe $+ ZrB_{12}$, where a and a″ are amorphous phases, and a′ can be indexed as a γ-Fe (fcc) structure, with a crystalline order on an average distance of 8 Å. The metallic glass demixed on quenching, but component phases tended to mix by exchanging Fe atoms in a temperature range overlapped with the first crystallisation, which yields α-Fe nanocrystals (≈27 Å). Higher temperature exo-peaks correspond mainly to a recrystallisation of the phases formed at lower temperature. It was found that this alloy has nanocrystalline structure also after heating at a well higher temperature than first crystallization. Even after the last exo-peak, the average crystallite size (*D*) was considerably smaller than that found in the literature for analogous metallic glasses; *D* values for our alloy were comparable to those of nanocrystalline phases of other systems heat treated below the temperature of exothermal DTA peaks. Extensive oxidation above 600°C, even at a low oxygen content ($c_{o_2} \leq 2$ ppm), led to a marked modification of the surface layer: two zirconia polymorphs were identified on the surface of the ribbons, and the ratio of γ-Fe to α-Fe content increased with respect to the bulk. Differences in thermal evolution between outer layer and bulk are attributed to a different phase composition and non-uniform distribution since the as-quenched stage.

1. Introduction

Amorphous ferromagnetic alloys produced by rapid quenching from a melt show several interesting features concerning thermal evolution from a disordered to an ordered structure [1], and correlation among structural relaxation, nanocrystallization and very soft magnetism [2]. In addition, possible applications in delay lines and sensor devices have been envisaged [3]. Metallic melt casting requires very high quenching rates if amorphous alloys are to be produced. Recently it was shown that glasses of general formula $Fe_{56}Co_7Ni_7Zr_{10-x}Nb_xB_{20}$ have a wide supercooled liquid region [4], which is a basic requirement for a high thermal stability of the supercooled phase against crystallization. In addition, promising soft magnetic properties have been found for these alloys [5].

These results were confirmed for the amorphous alloy of composition $Fe_{62.5}Co_6Ni_{7.5}Zr_6Nb_2Cu_1B_{15}$, which was specifically designed for application in magnetoelastic devices [6, 7]. The present work concerns this new alloy, and was aimed at understanding the stability conditions of the disordered structure in view of the optimisation for applications.

2. Experimental

The amorphous alloy was prepared by one-roll melt-spinning technique, with a quenching rate of 28 m/s, starting from a precursor alloy produced by arc melting in a quartz crucible by Ar gassing. Samples of $Fe_{62.5}Co_6Ni_{7.5}Zr_6Nb_2Cu_1B_{15}$ were in the shape of ribbons: 30 μm × 3 mm × several metres. The composition of the specimens was checked by wavelength dispersive Electron Scanning Microscopy Analysis (ESMA).

Differential Thermal Analysis (DTA) was carried out by means of a Netzsch heat flux DSC apparatus (model 404M) on ∼50 mg samples at various heating rates (2–80°C/min). The reference material was powdered Al_2O_3. Thermogravimetric analysis (TG) was carried out by means of a Netzsch Thermo-Microbalance apparatus (model TG209) on about 15 mg of powdered sample. The sample was heated at a heating rate of $\beta = 20°\text{C/min}$ in argon atmosphere.

XRD patterns were collected on a PMG-VH Rigaku diffractometer using the conventional Bragg-Brentano geometry. The system was equipped with a diffracted beam graphite crystal analyser, and suitably narrow slits (Soller, incident, divergence and antiscattering) so as to produce a nearly zero background and narrow and symmetrical instrumental profiles, even for 2θ angles as low as 20–25°[8]. The Instrumental Resolution Function (IRF), describing the change in profile width and shape with the 2θ angle was determined using a suitable KC1 powder sample, and analytically described by means of a non-linear least square fitting of pseudo-Voigt functions for the CuKα_1, α_2 doublet [8, 9].

The XRD patterns were analysed by a commercially available Search-Match program for phase identification, whereas lattice parameter, line profile analysis and quantitative phase analysis of Fe polymorphs were obtained by using a recently developed computer program based on the Rietveld method [10], which is specifically designed to allow a simultaneous refinement of structural and microstructural parameters, including domain size and lattice defects. Details on the program and algorithm can be found in the cited literature [10–12]. Finally, lattice parameters of α-Fe and γ-Fe in powder samples were obtained by using a Si internal standard, mixed with the ground ribbon.

AFM analysis of the ribbons surface topography was performed by means of Lot Oriel apparatus both in tapping mode and in contact one.

3. Results

The DTA curve recorded at 20°C/min is reported in Fig. 1. On heating the alloy undergoes a complex crystallisation process, in several steps corresponding to the various exo-peaks. The two slope changes in the curve, before the first exo-peak, in the temperature range 400–500°C, can be related to the changes of specific heat in the glass transformation temperature range. The occurrence of two glass transformation effects indicates a glass-in-glass phase separation. Taking T_{g1} and T_x as the onset temperatures of the first slope change and exo-peak respectively, a temperature interval of supercooled liquid region $T_x - T_g = 123°\text{C}$ is obtained, which is larger than that ($45 \le T_x - T_g \le 85$) recorded for the above mentioned glasses [4, 5] of general formula $Fe_{56}Co_7Ni_7Zr_{10-x}Nb_xB_{20}$, having a lower Fe but a higher B + Zr content.

A sample was also submitted to a thermogravimetric (TG) analysis (both DTA and TG were done in Ar atmosphere), with an oxygen level $c_{O_2} \le 2$ ppm. The TG curve is reported in Fig. 1. As can be seen, a weight increase is recorded starting from $T = 580°\text{C}$ in the temperature range of the second exo-peak. The occurrence of an oxidation at such a low O_2 level is not surprising in the light of the results of previous work [13].

The XRD patterns of samples variously heat treated are reported in Figs 2 and 3. The as-cast sample (Fig. 2a) confirmed to be amorphous. Fig. 2b–d refer to samples submitted, in the DTA apparatus, to non-isothermal heat treatments stopped respectively, at the first and second peak, and after the last exo-peak. A broad XRD reflection is present in the pattern 2b, corresponding to the strongest line of α-Fe. In Fig. 2c (2nd exo-peak) this reflection becomes sharper and a second one appears at $2\theta \cong 28$ with other minor peaks at ~30.2 and 35.2°. In the XRD pattern of the sample heated up to 750°C (Fig. 2d) the reflections of γ-Fe also appear clearly.

The brittleness induced by crystallisation, allowed sample grinding. The XRD patterns of powdered samples are reported in Fig. 3. Fig. 3a and b, relative to DTA stopped at the first and second exo-peak, confirm the results reported in Fig. 2, apart from the absence of the reflection at $2\theta \sim 28°$. The first DTA crystallisation peak corresponds, therefore, to the formation of very fine crystals of α-Fe giving broad XRD reflections; the second DTA peak corresponds to the growth of this crystalline phase, whose reflections become sharper. The XRD spectra performed before (3d) and after (3c) grinding the sample heated in the DTA apparatus at

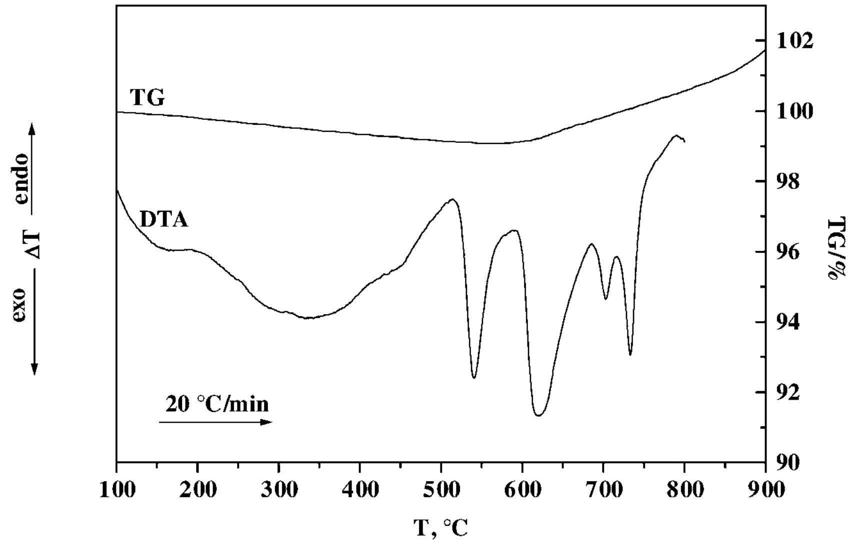

Figure 1 Differential thermal analysis (DTA) and thermogravimetric (TG) curves recorded at 20°C/min.

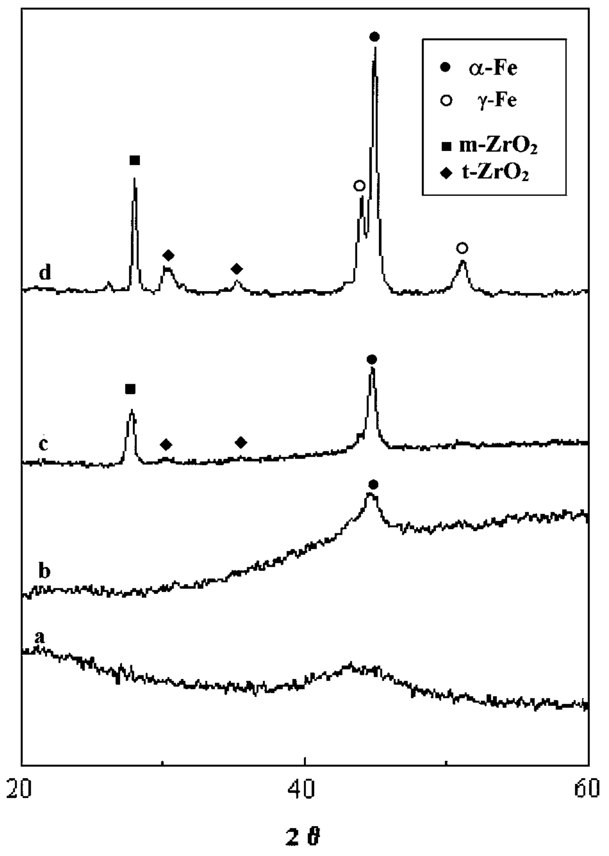

Figure 2 XRD patterns of samples as quenched (a) and submitted (b–d) to DTA cycle stopped at: (b) I exo-peak; (c) II exo-peak; (d) after the last exo-peak.

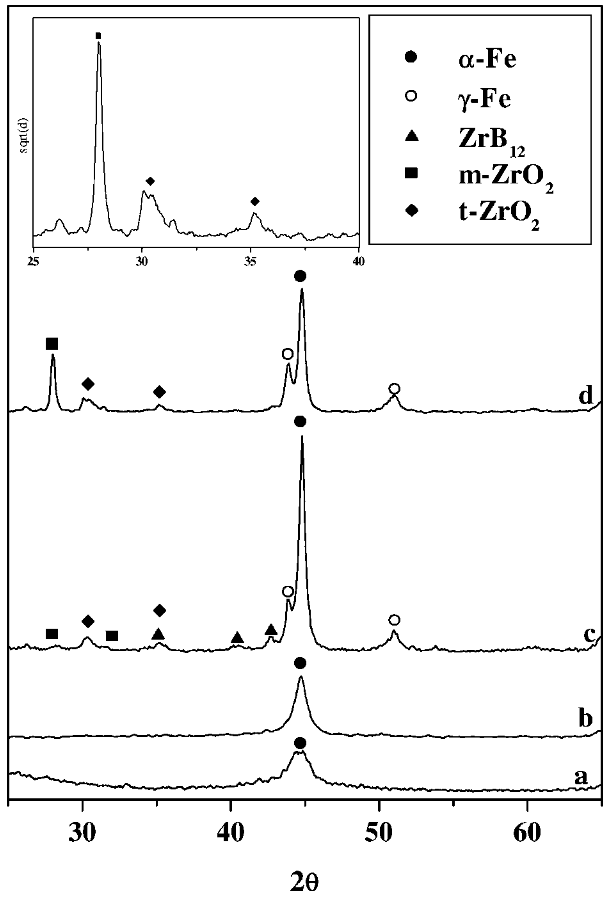

Figure 3 XRD patterns of powders obtained by grinding samples submitted to DTA cycle stopped at: (a) I exo-peak; (b) II exo-peak; (c) after the last exo-peak; Sample (d) refers to a sample submitted to XRD as ribbon. A particular of Fig. 3d is also reported.

$\beta = 20°\text{C/min}$ to 750°C (i.e., up to the end of the last exo-peak) show several interesting differences:

(a) peak at $2\theta \cong 280$ is absent in the ground sample;
(b) the ratio between γ-Fe and α-Fe peak areas increases in the ribbon (3d) sample;
(c) reflections of ZrB_{12} appear only in the pattern of the ground sample (3c);

The strong reduction of the $2\theta \cong 280$ reflection observed when the samples are powdered suggests that it corresponds to some oxidation product formed in the outer layer of the sample. Its appearance, starting from the 2c pattern, is otherwise consistent with the TG curve (Fig. 1) showing weight increases beginning at $T = 580°\text{C}$, which approximately corresponds to the onset of the second DTA exo-peak. The position of the observed XRD peak corresponds to that of the strongest line (111) of monoclinic ZrO_2 (m-ZrO_2); the absence of the other lines of m-ZrO_2 would imply an epitaxial growth of the oxide film. Reflections at $2\theta \cong 30.2$ and 35.2° can indeed be attributed to tetragonal ZrO_2 (t-ZrO_2) (*vide infra* of Fig. 3) (experimental evidence is not sufficient to distinguish between the tetragonal and the cubic zirconia polymorph: in the following we will refer to t-ZrO_2, but we cannot actually distinguish between the two high-symmetry polymorphs).

Recently a new model of line profile broadening due to the effect of linear and planar lattice defects was incorporated into the conventional Rietveld algorithm for the structural refinement and whole-pattern fitting of powder data [10–12]. The model was used to fit the XRD patterns in order to evaluate lattice parameter, a, average domain size, D and microstrain due to lattice defects. The α-Fe and γ-Fe percentage amounts were evaluated by considering the two phases as made of pure iron and neglecting the presence of the other crystalline phases. Fig. 4 shows the good quality of the fitting. The values of a, D, microstrain and relative amounts of α-Fe and γ-Fe are reported in Table I. As can be seen, the value of the lattice parameter of α-Fe does not depend on the heat treatment and is close to the standard value for pure iron ($a = 2.866$ Å). The value for γ-Fe, instead, changes greatly as a function of the thermal treatment.

If we compare these results with those found in the literature for other amorphous alloys, it turns out that the average crystalline-domain size after each crystallisation step is very small. Even after the last exo-peak, D values are lower than those found for other devitrified metallic glasses; grain size, in fact, is comparable to that of nanocrystalline phases obtained in other amorphous alloys but only by annealing at temperatures lower than those of DTA exothermal peaks [14].

DTA curves recorded at various heating rates (2–80°C/min) are reported in Fig. 5. They show an unusual behaviour, already observed for the $Fe_{73.5}Si_{13.5}B_9Nb_3Cu_1$ alloy [15]: the ratio between I and II peak areas changes with the heating rate. In the previous work [15], DTA showed only two exo-peaks and a maximum in the plot of the ratio between I and II peak areas versus heating rate (β). In the present

TABLE I Lattice parameter, a, average domain size, D, microstrain, α-Fe and γ-Fe %amounts in the thermally treated samples

	a(Å)		D(Å)		Vol%		Weight%		Microstrain	
Sample	γ-Fe	α-Fe	γ-Fe	α-Fe	γ-Fe	α-Fe	γ-Fe	α-Fe	γ-Fe	α-Fe
(a) Powders 20°C/min I-exo	3.70	2.8679	8	27	36.5	63.5	34.5	65.5	0	0
(b) Powders 20°C/min II-exo	3.644	2.8691	30	51	10	90	9.8	90.2	0	0
(c) Powders 20°C/min Completely devitrified	3.581	2.8693	90	155	27	73	28.1	71.9	0	26×10^{-4}
(d) Powders 80°C/min Completely devitrified	3.582	2.872	165	98	17.2	81.8	17.7	81.3	18×10^{-4}	58×10^{-4}
(e) Ribbons 80°C/min Completely devitrified	(3.581)	2.8705	135	132	54.7	45.3	56.3	43.7	12×10^{-4}	16×10^{-4}

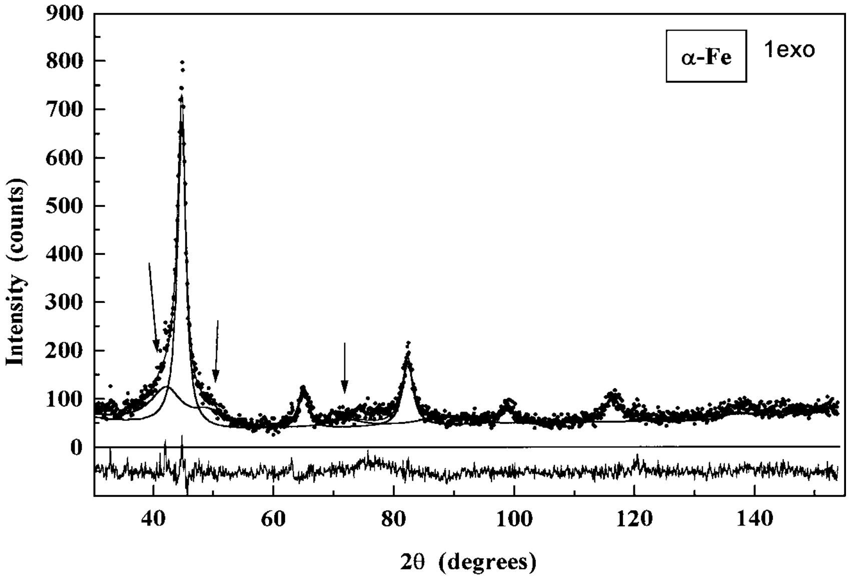

Figure 4 XRD patterns of Fig. 3a with fitting curve. The reflection of γ-Fe are indicated by the arrows. In the bottom the difference of the experimental and fitting spectra is reported.

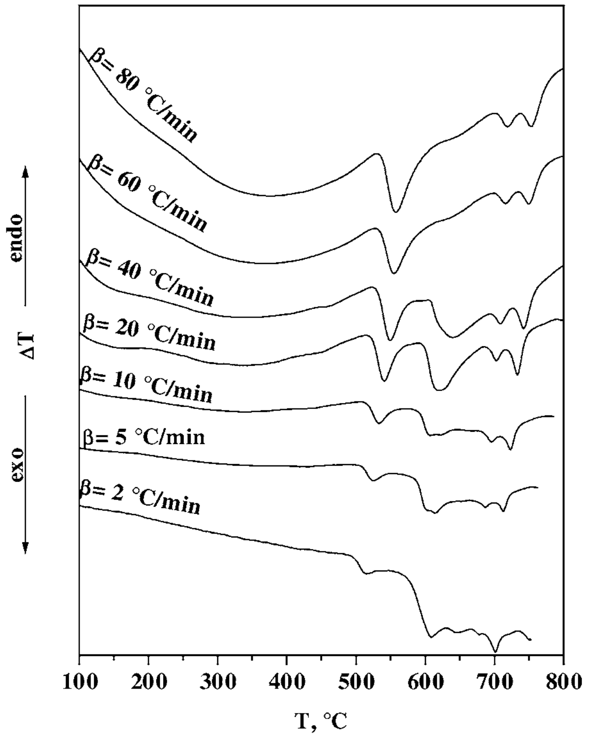

Figure 5 DTA curves recorded at the heating rates reported on the curves.

case the ratio between II and I peak area decreases with β. At $\beta = 80$°C/min the II peak almost disappears.

The XRD patterns of a sample submitted to a DTA recorded at 80°C/min and stopped after the last exo-peak (i.e., completely crystallised) are reported in Fig. 6. Also in this case XRD was performed twice: before (Fig. 6d) and after (Fig. 6b) grinding. Values of lattice parameter (a), average domain size (D) and microstrain due to lattice defects obtained from the pattern fitting procedure are reported in Table I.

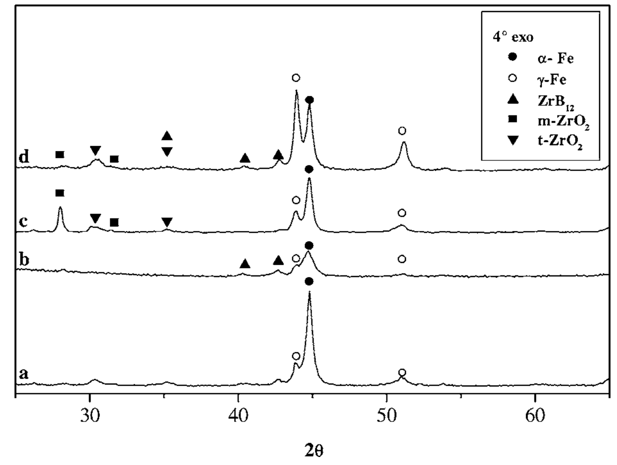

Figure 6 XRD patterns of samples submitted as ribbons to DTA: 80°C/min before (d) and after (b) grinding; 20°C/min before (c) and after (a) grinding.

The AFM picture in Fig. 7 clearly shows nearly equiaxial grains, on a sub-micron scale, covering the surface of a ribbon heat-treated for 1 h at 400°C. In addition, several acicular grains lay above the fine-grain layer, or are partially embedded.

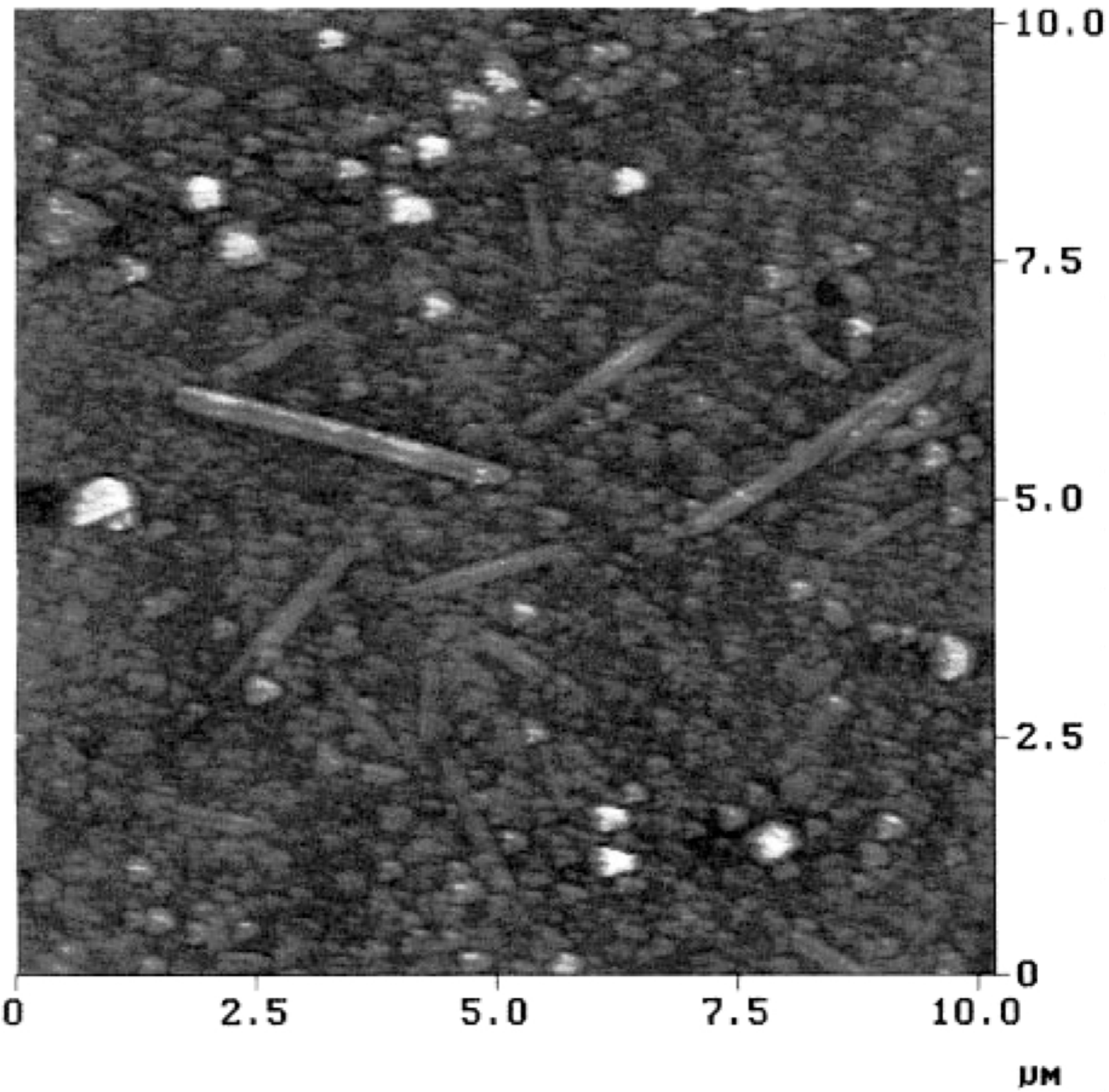

Figure 7 AFM micrograph of as sample annealed 1 h at 400°C.

4. Discussion

Rapid quenching of metallic melts gives amorphous alloys with a more or less large excess-volume; when heat-treated in the glass transformation temperature range they undergo crystallisation. However, important structural changes occur at lower temperatures where long range diffusion is hindered. At these temperatures there may be several kinds of short-range ordering of topological (TSRO) or chemical (CSRO) nature [16, 17]. Moreover glasses before crystallisation can undergo, in the glass transformation temperature range, a more or less extensive glass-in-glass phase separation [18]. When metastable immiscibility occurs, a consolute temperature is defined above which no demixtion occurs. Below this temperature the composition and relative amounts of the glass-in-glass separated phases depend on the temperature and on the nominal composition of the glass. Many glasses demix on quenching.

The presence in the DTA curve reported in Fig. 1 of two slope changes, before the first crystallisation exo-peak, suggests that the metallic glass is demixed into at least two amorphous phases. The crystallisation process is complex and occurs in several steps.

The XRD pattern of Figs 2b and 3a clearly show that the first exo-peak corresponds to the crystallisation of α-Fe. The results of the modelling shown in Fig. 4 and reported in Table I indicate the presence of another phase, resembling the lattice structure of γ-Fe, which exhibits a crystalline order on an average distance of 8 Å. The particularly large lattice parameter suggests that this phase would accommodate foreign atoms (Co and Ni are preferentially hosted by the γ-Fe).

The diffraction patterns of Figs 2c and 3b where collected on samples whose heating was stopped at the II exo-peak. As discussed above, the reflection at $2\theta \sim 28°$ in the ribbon pattern is attributed to m-ZrO_2. As shown in the Table I, crystal size and percentage of α-Fe in sample b) increase with respect to sample a). If the alloy demixed on quenching, the recorded structural change could be due to some mixing, involving the exchange of Fe atoms that would allow the α-Fe crystals to grow further. The other phase is deeply modified: γ-Fe nanocrystals of average size 30 Å form, and lattice parameter is 3.644 Å instead of 3.700 Å.

At higher temperature ZrB_{12} forms (Fig. 3c). In addition, the following points are of interest:

(a) the microstrain in the α-Fe crystalline phase increases from 0 to 2.6×10^{-3};

(b) the lattice parameter of γ-Fe decreases from 3.644 Å to 3.581 Å.

These results suggest that in the higher temperature range a recrystallisation of the α and γ phases occurs. It is also observed (see Table I) an increase in both γ/α amount ratio and crystal size of both crystalline phases. The increase in γ/α ratio is consistent with the fact that γ-Fe is the high temperature polymorph.

The crystallisation process can be summarised as follows:

$$\begin{aligned} &\mathrm{a} \rightarrow \mathrm{a}' + \alpha\text{-Fe} \rightarrow \mathrm{a}'' + \alpha\text{-Fe} + \gamma\text{-Fe} \\ &\quad \rightarrow \alpha\text{-Fe} + \gamma\text{-Fe} + \mathrm{ZrB}_{12} \end{aligned}$$

where a and a$''$ are amorphous phases, a$'$ appears to have a crystalline order on an average distance of 8 Å, resembling the lattice structure of γ-Fe.

The unusual behaviour shown in Fig. 4, i.e. the dependence of the DTA exo-peak areas on β, can also be explained if we assume that the alloy is demixed on quenching, but the relevant phases tend to mix by exchanging Fe atoms in a temperature range overlapped with that of the first crystallisation. Taking into account that, as usual, the effect of increasing the DTA heating rate is to shift crystallisation towards higher temperatures, one could speculate that the higher the heating rate the more extensive exchange of Fe atoms would occur between the amorphous phases before any crystallisation takes place. Therefore, the greater β the lower is expected to be the ratio between second and first exo-peak area.

When comparing Figs 6c and 6d, the difference in the intensity of the ZrO_2 phase reflections indicates, as expected, that samples submitted to DTA are less oxidised, the higher is the heating rate. In this context, it is worth noting that the γ/α ratio in Fig. 6a–d changes considerably; a higher γ/α ratio in the ribbons XRD spectra could well be due to some equilibrium shift caused by the oxidation of the outer layers. However, the fact that γ-Fe is dominant in the 6d spectrum, which refers to the less oxidised sample, suggests the existence of some difference, in the as quenched sample, between the phase composition of outer layer and bulk.

The morphological information of Fig. 7, compared with the XRD results of phase identification, supports the hypothesis that t-ZrO_2 and m-ZrO_2 tend to form on the surface of the ribbons owing to the oxidation. As also suggested by the broadening of the XRD profiles, t-ZrO_2 grains are quite small, whereas m-ZrO_2 is more likely to be present in the shape of larger crystals, with a marked texture. In fact, in the XRD pattern of a ribbon after IV exo-peak (Figs 2d or 3d or 6c)—we can find only a quite strong and narrow reflection from the monoclinic phase, corresponding to the $(\bar{1}11)$ planes, which is what we should observe in case of a strong texture like that of the acicular grains displayed by the AFM picture.

In the pattern of the powdered samples (Fig. 3c) the two oxide phases are also visible, but the reflections are weaker than in the ribbon, suggesting that most (or all) the oxide grains formed on the surface of the ribbons. Moreover, at least two m-ZrO_2 reflections are visible ($(\bar{1}11)$ and (111)), since grinding the ribbons obviously destroyed texture.

As a final comment concerning the simultaneous presence of two zirconia polymorphs, it is worth noting that this is not an unusual result in zirconia-containing materials [19]. m-ZrO_2 is the stable phase at room temperature, but the presence of some oxides, leading to a substitution in the cation lattice of zirconia and/or to vacancies in the anion lattice, can stabilise t-ZrO_2 as well as c-ZrO_2. In addition, the two high symmetry phases can be stabilised below a critical grain size [20].

5. Conclusions

The crystallisation of the studied metallic glass, on heating in a DTA apparatus, occurs in several steps. The process can be summarised as follows:

$$\begin{aligned} &\mathrm{a} \rightarrow \mathrm{a}' + \alpha\text{-Fe} \rightarrow \mathrm{a}'' + \alpha\text{-Fe} + \gamma\text{-Fe} \\ &\quad \rightarrow \alpha\text{-Fe} + \gamma\text{-Fe} + \mathrm{ZrB}_{12} \end{aligned}$$

where a and a$''$ are amorphous phases, and a$'$ can be indexed as a γ-Fe (fcc) structure, with a crystalline order on an average distance of 8 Å.

α-Fe nanocrystals (average size of the order of 27 Å) are obtained in the first crystallisation step. Some experimental results, however, suggest that the metallic glass demixed on quenching, but that the demixed phases probably tend to mix by exchanging Fe atoms in a temperature range overlapping that of the first crystallisation. The higher temperature exo-peaks correspond mainly to a recrystallisation of the phases formed at a lower temperature.

The average crystallite size (D) after each crystallisation step is very small as compared with corresponding values found in the literature. Even after heating the alloy up to 750°C, corresponding to the last exo-peak, D is considerably smaller than in similar metallic glasses, which, at this temperature are micro- or macro-cristalline. Similar grain sizes were previously observed only annealing at temperatures well below exothermal DTA peaks ($T \leq 560°\mathrm{C}$ in Finemet). Starting from 600°C an important oxidation process occurs, even at very low oxygen content ($c_{O_2} \leq 2$ ppm), leading to a surface layer with a different phase composition than in the bulk of the metallic glass ribbons. In this surface layer monoclinic and tetragonal ZrO_2 form as the primary oxidation product, ZrB_{12} is absent, and the ratio between the amount of γ-Fe and α-Fe phases increases with respect to the bulk. The different thermal evolution of outer layer and bulk can be attributed to differences in the phase composition already present in the as-quenched ribbons.

Acknowledgments

The work was supported by the National Institute for Matter Physics (INFM) as part of the project for 'Magnetoelastic sensors production for the measure of displacements, vibrations and mass flows'.

References

1. S. SCHNEIDER, U. GEYER, P. THIYAGARAJAN and W. L. JOHNSON, *Mater. Sci. Forum* **235–238** (1997) 337.
2. A. GONZALES, A. ZERN and A. HERNANDO, *J. Magn. Magn. Materials* **196/197** (1999) 175.
3. H. CHIRIAC, E. HRISTOFOROU, M. NEAGU, F. BARARIU and T. A. OVARI, *J. Appl. Phys.* **85** (1999) 5729.
4. A. INOUE, H. KOSHIBA, T. ZHANG and A. MAKINO, *ibid.* **83**(4) (1998) 1967.
5. J. TAKAHOMI and A. INOUE, *Appl. Phys. Lett.* **74** (1999) 25/D.
6. L. LANOTTE, V. IANNOTTI and M. MÜLLER, *Int. J. Appl. Electromagnetics and Mechanics* **10** (1999) 215.
7. L. LANOTTE, G. AUSANIO, M. CARBUCICCHIO, V. IANNOTTI and M. MÜLLER, in Proceedings of SMM14 "Soft Magnetics Materials 14", Balatonfüred, Ungheria, Sept. 8–10, 1999.
8. P. SCARDI, L. LUTTEROTTI and P. MAISTRELLI, *Powder Diffraction.* **9**(3) (1994) 180.
9. M. LEONI, P. SCARDI and J. I. LANGFORD, *ibid.* **13**(4) (1998) 210.
10. P. SCARDI, in "X-ray Powder Diffraction Analysis of Real Structure of Matter," edited by H.-J. Bunge, J. Fiala and R. L. Snyder, IUCr series (Oxford Univ. Press, 1999) p. 570.
11. M. LEONI and P. SCARDI, *Mat. Sci. Forum* **278–281** (1998) 177.
12. P. SCARDI and M. LEONI, *J. Appl. Cryst.* **32** (1999) 671.
13. J. FUSY and P. PAREJA, *J. Non. Cryst. Solids* **89** (1987) 131.
14. G. HERZER, *J. Magn. Mater.* **112** (1992) 258.
15. F. BRANDA, A. COSTANTINI, L. LANOTTE and P. MATTEAZZI, *J. Mat. Sci.* **32** (1997) 6015.
16. P. H. GASKELL, *J. Non-Cryst. Solids* **32** (1979) 207.
17. H. HERMAN and W. KREHER, *J. Phys. F: Met. Phys.* **18** (1988) 641.
18. Z. STRNAD, in "Glass-Ceramic Materials" (Elsevier, Amsterdam, 1986).
19. M. LEONI, R. L. JONES and P. SCARDI, *Surf. Coat. Technol.* **108/109** (1998) 107.
20. R. C. GARVIE and M. F. GOSS, *J. Mater. Sci.* **21** (1986). 1253.

Received 6 November 2000
and accepted 1 October 2001